NeuroImage 263 (2022) 119663

Contents lists available at ScienceDirect

NeuroImage

journal homepage: www.elsevier.com/locate/neuroimage

Reliability and similarity of resting state functional connectivity networks imaged using wearable, high-density diffuse optical tomography in the home setting

Julie Uchitel[a,#,*], Borja Blanco[a,b,#,**], Ernesto Vidal-Rosas[a], Liam Collins-Jones[a], Robert J. Cooper[a]

[a] DOT-HUB, Department of Medical Physics and Biomedical Engineering, UCL, London, United Kingdom
[b] Department of Psychology, University of Cambridge, Cambridge, United Kingdom

ARTICLE INFO

Keywords:
High-density diffuse optical tomography
HD-DOT
Wearable neuroimaging
Reliability
Similarity
Resting-state functional connectivity
Functional brain networks
Home setting

ABSTRACT

Background: When characterizing the brain's resting state functional connectivity (RSFC) networks, demonstrating networks' similarity across sessions and reliability across different scan durations is essential for validating results and possibly minimizing the scanning time needed to obtain stable measures of RSFC. Recent advances in optical functional neuroimaging technologies have resulted in fully wearable devices that may serve as a complimentary tool to functional magnetic resonance imaging (fMRI) and allow for investigations of RSFC networks repeatedly and easily in non-traditional scanning environments.

Methods: Resting-state cortical hemodynamic activity was repeatedly measured in a single individual in the home environment during COVID-19 lockdown conditions using the first ever application of a 24-module (72 sources, 96 detectors) wearable high-density diffuse optical tomography (HD-DOT) system. Twelve-minute recordings of resting-state data were acquired over the pre-frontal and occipital regions in fourteen experimental sessions over three weeks. As an initial validation of the data, spatial independent component analysis was used to identify RSFC networks. Reliability and similarity scores were computed using metrics adapted from the fMRI literature.

Results: We observed RSFC networks over visual regions (visual peripheral, visual central networks) and higher-order association regions (control, salience and default mode network), consistent with previous fMRI literature. High similarity was observed across testing sessions and across chromophores (oxygenated and deoxygenated haemoglobin, HbO and HbR) for all functional networks, and for each network considered separately. Stable reliability values (described here as a <10% change between time windows) were obtained for HbO and HbR with differences in required scanning time observed on a network-by-network basis.

Discussion: Using RSFC data from a highly sampled individual, the present work demonstrates that wearable HD-DOT can be used to obtain RSFC measurements with high similarity across imaging sessions and reliability across recording durations in the home environment. Wearable HD-DOT may serve as a complimentary tool to fMRI for studying RSFC networks outside of the traditional scanning environment and in vulnerable populations for whom fMRI is not feasible.

1. Introduction

Mapping the functional organization of the human brain at rest can be achieved through studies of resting-state functional connectivity (RSFC). RSFC is inferred from the synchronized activity of different brain regions at rest, such that regions exhibiting higher temporal synchronization can define RSFC networks. [Damoiseaux et al., 2006, Fransson et al., 2007] RSFC networks describe the intrinsic functional architecture of the brain, and are highly reflective of underlying structural connectivity. [Betzel et al., 2014, Honey et al., 2009] Typically,

Abbreviations: (HD-DOT), High-density diffuse optical tomography; (PFM), precision functional connectivity mapping; (fNIRS), functional near infrared spectroscopy; (RSFC), resting-state functional connectivity; (fMRI), functional magnetic resonance imaging; (HbO), oxygenated haemoglobin; (HbR), deoxygenated haemoglobin; (GM), grey matter; (sGICA), spatial group independent component analysis.

* Corresponding author at: University College London, Department of Medical Physics and Biomedical Engineering, London, United Kingdom.
** Corresponding author at: University of Cambridge, Department of Psychology, Cambridge, United Kingdom.
E-mail address: bb579@cam.ac.uk (B. Blanco).
# These authors have contributed equally to this work

https://doi.org/10.1016/j.neuroimage.2022.119663.
Received 10 February 2022; Received in revised form 28 September 2022; Accepted 2 October 2022
Available online 4 October 2022.

RSFC data are acquired from multiple individuals for short periods (5–20 minutes) in the absence of any explicit task or stimulus. Individual-level data are then co-registered to a common space, and RSFC networks are identified using the entire multi-subject dataset. By combining data from hundreds or even thousands of individuals, group-level studies of RSFC have allowed neuroscientists to map the functional organization of the human brain at rest in extraordinary detail. [Beckmann et al., 2005, Smith et al., 2009, Thomas Yeo et al., 2011]

In RSFC studies, subjects are often studied over a single testing session. However, identifying particular network features across repeated measurements (i.e., *similarity*) is key to ensure the accuracy and replicability of the obtained results. Furthermore, assessing the *reliability* of network features across different scanning durations can inform whether reliable measurements can be achieved from shorter recordings in the individual. This could be especially useful for studies involving developmental or clinical populations, for whom conducting long scanning sessions can be challenging, and has implications for the ease and regularity with which such measurements might be obtained.

While fMRI offers the advantage of high spatial resolution, its size and the requirement of the subject to remain still significantly limit its application to vulnerable populations, such as critical care patients or infants, and to ecologically meaningful contexts. Furthermore, fMRI has contraindications for subjects with electronic or metal implants (such as pacemakers, cochlear implants, aneurysm clips, and surgical devices). Neuroimaging methods that are portable and even wearable have the potential to allow investigations of RSFC in these populations and in unrestricted environments, such as at the bedside, in the clinic, or in the home.

Functional near-infrared spectroscopy (fNIRS) surmounts many of these challenges by allowing for studies of cortical activity outside of the traditional scanning environment. [Boas et al., 2014] fNIRS employs an array of optical sources and detectors placed on the scalp to monitor the changes in the cerebral concentrations of oxyhaemoglobin (HbO) and deoxyhaemoglobin (HbR). Several previous studies have employed fNIRS to investigate RSFC in the adult [Racz et al., 2018, Zhang and Zhu, 2020, Niu et al., 2019, Li et al., 2015, Lu et al., 2010, Niu et al., 2013] and infant brain. [Homae et al., 2010, Taga et al., 2018, Blanco et al., 2021, Lee et al., 2020]

An extension of fNIRS known as diffuse optical tomography (DOT) uses multiple sources and detectors of near-infrared light at several source–detector distances to acquire images of HbO and HbR changes over the cortical surface. [Pinti et al., 2020, White et al., 2009, Eggebrecht et al., 2014, Chalia et al., 2019] High density DOT (HD-DOT) [White and Culver, 2010, Vidal-Rosas et al., 2021, Frijia et al., 2021] takes the method further still. Using a dense array of channels with spatially overlapping sensitivity distributions and a range of source-detector separations, spanning the “short separation” (<15 mm) to “long” (≥30 mm) range, HD-DOT permits the production of high-quality three-dimensional images of functional brain activity. The information obtained from the plurality of overlapping channel measurements increases spatial resolution, and the use of multiple source–detector separations improves depth specificity, [White and Culver, 2010] though as with all existing optical neuroimaging methods, the sensitivity of HD-DOT is limited to the superficial areas of the cortex.

Several prior fNIRS and DOT studies have investigated similarity and reliability of network metrics across testing sessions and scanning durations. Geng et al. (2017) investigated the effect of fNIRS scanning duration on a set of graph theory metrics derived from RSFC data. [Geng et al., 2017] Nodal efficiency (a measure of the ability of a node to propagate information with the other nodes in a network) and nodal betweenness (a measure of centrality in a network) were found to be reproducible after only one minute of fNIRS signal acquisition, whereas local and global efficiency (both measures of efficiency in information transfer, locally and globally) were only reproducible after five minutes. Wang et al. (2017) assessed the minimum fNIRS scanning duration required to map stable RSFC and graph theory metrics in children. RSFC maps were stably achieved after seven minutes of scanning time, while graph metrics were stably achieved after two and a half minutes at low network thresholds. [Wang et al., 2017] White et al. (2009) developed the archetypal HD-DOT system, which was used to study RSFC networks in the adult human brain. [White et al., 2009] In this study, the system was used on a single adult subject and covered the motor and visual cortices. Recordings were performed across three sessions, and results suggested that RSFC maps could be produced with high similarity across sessions. While this study’s HD-DOT system provided large cortical coverage and high spatial resolution, the system’s bulky optical fibres limited translatability outside of the scanning environment and to certain populations.

Recently, our group demonstrated a new generation of wearable HD-DOT system (LUMO, *UCL DOT-HUB* and *Gowerlabs Ltd.,* UK). This system’s modular, lightweight design allows for large cortical coverage without sacrificing wearability, allowing for functional brain mapping to be undertaken outside of the traditional scanning environment. [Vidal-Rosas et al., 2021] We have demonstrated the feasibility of using a 12-module version of this system (36 sources and 48 detectors) for retinotopic mapping of the adult visual cortex [Vidal-Rosas et al., 2021] and social stimuli response mapping of the infant temporal cortex. [Frijia et al., 2021]

In the present study, we sought to demonstrate that a wide-field of view version of this same, wearable HD-DOT technology (comprising 24-modules, 72 sources and 96 detectors) can yield high similarity and reliability values in RSFC networks. Furthermore, we sought to demonstrate that it is possible to achieve this when the device is self-administered, and recording is undertaken in the home environment.

2. Materials and methods

2.1. Wearable HD-DOT system

We employed a custom 24-module HD-DOT system (LUMO, *UCL DOT-HUB* and *Gowerlabs Ltd.,* UK), [Vidal-Rosas et al., 2021, Frijia et al., 2021] constructed from two 12-tile LUMO systems run synchronously. The device consists of multiple, independent hexagonal modules (or ‘tiles’, **Fig. 1a**), each containing four photodiodes and three dual-wavelength LEDs emitting at 735 nm and 850 nm (24 modules yields 72 sources and 96 detectors total). The tiles are mounted into ‘docks’, and a chain (or chains) of docks are fitted into a neoprene cap. Seven short plastic optical fibres, one for each of the three sources and four detectors available in each tile, are mounted together to form a ‘light-guide’ that transmits light from the tile through the dock and hair to the scalp and back again. This scheme provides extensive flexibility to position the tiles to suit the experimental paradigm, while adapting to the curvature of the head. It also makes moving tiles from one cap to another fast and simple. **Fig. 1b** shows a 24-module array fitted within a neoprene cap, designed to interrogate the visual and pre-frontal cortices. This arrangement was chosen to assess easily mappable networks (visual networks and pre-frontal networks) as well as maximize the separation distance between the two LUMO dock chains to reduce the possibility of unwanted interaction effects between them. The full arrangement yields approximately 800 source-detector pairs (‘channels’, ~400 pre-frontal, ~400 occipital) within the 10–45 mm source-detector separation range expected to provide viable measurements.

2.2. Subject and experimental protocol

The study considered a single, healthy participant (author RJC, male, 36 years old at time of study) with normal vision and no known neurological conditions. Fourteen experimental sessions took place over a period of three weeks and under lockdown conditions due to the COVID-19 outbreak. The protocol employed was approved by the UCL research ethics committee under application 1133/001. However, as in this case

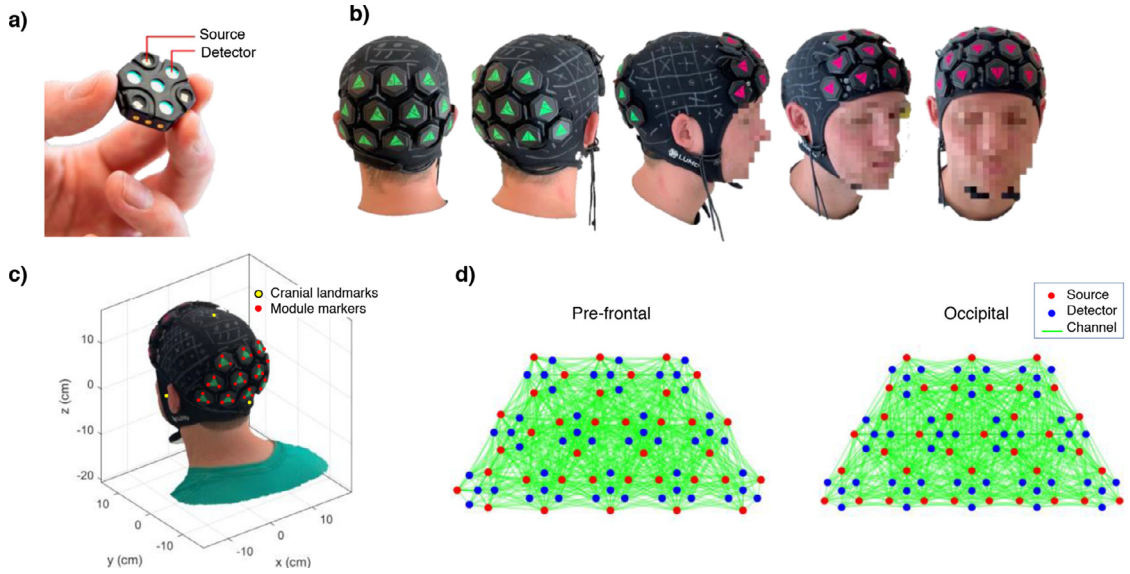

Fig. 1. Wearable HD-DOT system and registration. a) The LUMO tile module; b) neoprene cap fitted with a 24-module LUMO system and a subset of frames used during the photogrammetry process (de-identified), derived from a video recording that comprised three full rotations of the head at different heights; c) a final 3D surface mesh model of the participant's head showing the location of head landmarks (yellow circles) and module markers (red circles); d) source-detector and channel layout in pre-frontal and occipital regions showing channels with source–detector separation ≤40 mm. (For interpretation of the references to colour in this figure legend, the reader is referred to the web version of this article.)

the study was performed by the investigator on himself in a home environment, it was confirmed prior to commencement that the study fell outside the remit of the UCL research ethics committee. Each experimental session was carried out in a quiet and dimly lit room. First, the participant fitted himself with the neoprene cap and adjusted it with a Velcro chin strap. The cap was positioned to ensure that the same point on the cap (marked with a notch on the neoprene surface) was positioned over the inion, the distance of the cap above the ears was approximately equal on both sides, and the cap's frontline sat just above the eyebrows. The participant sat in an adjustable chair in front of a 27-inch computer monitor at a viewing distance of 90 cm; the full screen subtended a radial angle of 12°. A video recording of the participant for full length of the experiment was made to verify that he complied with the protocol, which included: sitting in a relaxed position, having full attention on the screen, and remaining awake and alert. All sessions were performed between 10:00–12:00 BST. Food and caffeine intake were also consistent, with the subject having had 1 cup of coffee and no food prior to recording. Each resting-state recording session lasted twelve minutes during which the subject attended to a fixation cross displayed on a 50% grey background. [Vidal-Rosas et al., 2021]

2.3. Optode registration

The 3D digitization of the optode locations was performed using photogrammetry. [Vidal-Rosas et al., 2021] Briefly, the registration process began by having a second individual record a video of the participant using a smartphone (iPhone XR, Apple Inc.). This video consisted of three panning rotations around the subject's head at different heights (**Fig. 1b**), while the participant was seated and still with their eyes closed. The video was imported into a commercial photogrammetry software package (Metashape, *Agisoft LLC*), where between 140 and 200 frames were automatically extracted and used to produce a three-dimensional mesh model. A custom-made program written in MATLAB (*MathWorks, Inc.*) allowed the manual selection of the locations of the cranial landmarks and tile markers (the corner of green and pink triangle stickers on the HD-DOT modules) that were then used to determine the location of the sources and detectors on the subject's scalp. An example of the participant's digitized head model is displayed in **Fig. 1c**, along with the cranial landmarks (yellow circles) and tile marker positions (red circles). Since the dimensions of the tiles and light guides are fixed and known, the location of the seven optical contact points on the scalp could be computed from the locations of the tile marker positions without further approximation. **Fig. 1d** shows the array layout for pre-frontal and occipital regions.

2.4. Head modelling and registration

MRI images of the participant were available from a previous experiment. [Zhao et al., 2020] This provided T_1- and T_2-weighted magnetic resonance (MR) images that were linearly co-registered [Avants et al., 2011] and used to obtain a five-layer tissue head model using the unified segmentation algorithm. [Ashburner and Friston, 2005] The head model included scalp, skull, cerebrospinal fluid (CSF), grey matter (GM), and white matter (WM) tissue layers, which were converted into a high-resolution tetrahedral mesh using *Iso2mesh* (github.com/fangq/iso2mesh), a MATLAB mesh generation and processing toolbox. [iso2mesh 2020] The head volume mesh contained $\sim 2 \times 10^6$ elements and $\sim 3 \times 10^5$ nodes. The mesh included the MRI-derived cranial landmarks, which were used to register the digitized source and detector positions onto the surface of the mesh by means of a rigid transformation. Additionally, a surface mesh of the GM was built to aid visualisation of the imaging results. The pipeline for the registration process is illustrated in **Fig. 2**.

2.5. Signal processing and HD-DOT image reconstruction

Each step in the data pre-processing pipeline was undertaken using functions from the Homer2 fNIRS processing package (www.homer-fnirs.org), or modified versions thereof. Channels were discarded if their mean intensity values fell outside of the range of 5×10^{-5} V to 2.5 V; if their coefficient of variation (standard deviation/mean intensities) exceeded 8%; or if they were outside of the distance range of 0–60 mm. Intensity data were then converted to absorbence (optical density, OD) and then to changes in oxy- and deoxy-haemoglobin concentrations (HbO and HbR). Motion correction was not used in preprocessing given that the data were motion free as per visual inspection (see **Supplementary Figures 1–4**), the benchmark adult RSFC HD-DOT study did not

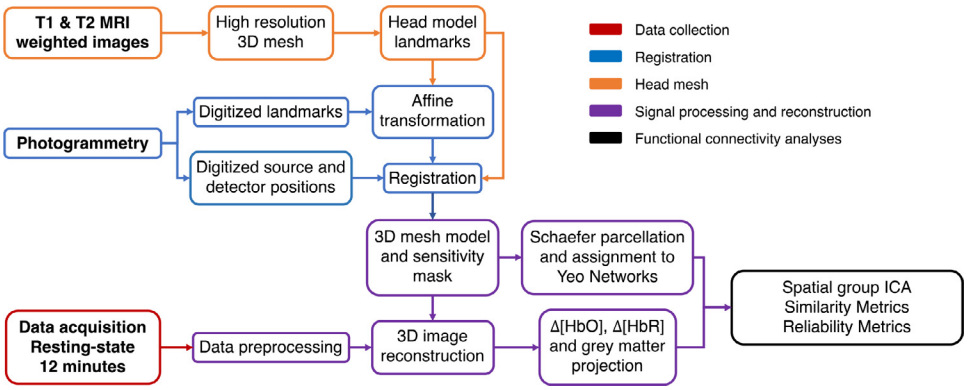

Fig. 2. Data collection and analysis pipeline. Pipeline for head modelling, registration, data preprocessing, and the reconstruction of images of hemodynamic changes.

use motion correction, [White et al., 2009] and the effects of motion correction techniques on data and results are variable. [Cooper et al., 2012, Sherafati et al., 2020] To account for extracerebral contamination, we employed a local short-separation regression approach. [Vidal-Rosas et al., 2021] In this approach, the average of the signals derived from all the short channels that share the source or the detector of a given long channel are regressed from the signal of that long channel. The rationale behind this approach is that extracerebral contamination of a long-channel signal is primarily due to changes in haemoglobin concentrations directly beneath its source and its detector, [Gagnon et al., 2012] and thus the single short channel closest to the mid-point of that long channel (which is typically used as a regressor) is unlikely to be the optimal choice. Following short separation regression, temporal filtering to the RSFC range was performed using a nuisance regression model. [Caballero-Gaudes and Reynolds, 2017] Sine and cosine functions for frequencies above 0.08 Hz were included in the model to remove the contribution of physiological noise sources (e.g., respiration and cardiac pulsation), and up to 5th order Legendre polynomials were included to account for fluctuations at very low frequencies. Finally, data were downsampled to one-fourth of the original frequency (to 1.25 Hz) to reduce data dimensionality for image reconstruction.

For image reconstruction, the forward problem was modelled using the diffusion approximation. [Arridge, 1999] The Jacobian matrix was calculated using the discretized diffusion equation using the finite element method in Toast++ [Schweiger and Arridge, 2014] which was applied to our subject-specific head mesh. The Jacobian was calculated in a fine regular grid with size of $30 \times 30 \times 30$ voxels and then projected into the tetrahedral head model. [Schweiger and Arridge, 2003] The optical properties of each tissue layer of the mesh were derived from literature values, [Bevilacqua et al., 1999] linearly interpolated to provide values at the required wavelengths. Images of changes in absorption coefficient were calculated via inversion of the forward model using zeroth-order Tikhonov regularization. The recovered images of the changes in absorption coefficient at the two wavelengths were then converted to images of changes in HbO and HbR concentrations. [Cope, 1991] For visualization and further analysis, these haemoglobin images were then mapped from the tetrahedral volume mesh to the GM surface mesh. Following this, a sensitivity map of the array setup was calculated by first finding a sensitivity mask for each individual session. To create a sensitivity mask for each session, we set a threshold of 5% of the maximum value of the normalized Jacobian such that nodes exhibiting a sensitivity above this value were set equal to one in a binary mask. All sessions' binarized masks were then summed to compute a group-level mask.

2.6. Cortical parcellation

In the image space, computing HbO and HbR functional connectivity (FC) matrices based on tens of thousands of GM surface mesh nodes is highly computationally expensive. To reduce data dimensionality, a cortical parcellation approach was used. In this approach, the GM surface mesh is divided into parcels. The HbO and HbR values for all nodes within each parcel are averaged to produce a single HbO and HbR value for each parcel at each time point. In this study, the Schaefer atlas [Schaefer et al., 2018] was used for parcellation as it is based on both anatomical and functional information. The atlas comprises 1000 parcels across the brain volume and was developed from the application of gradient-weighted Markov Random Field model to the MRIs of 1489 participants. For this study, the Schaefer atlas, which exists in the same space as the Colin27 model, [Collins et al., 1994] was converted from voxel form to node positions. We non-linearly registered the T_1-weighted Colin27 MRI template to the space of the participant's T_1-weighted MR image. This transform was used to transform the node positions from the Schaefer parcellation to the space of the subject. Each node in the participant's GM surface was assigned an anatomical label according to the label of the nearest transformed node from the Schaefer atlas.

The group level sensitivity mask was then applied to the parcellated GM surface mesh, producing a map of parcels that the array was sensitive to (**Fig. 3**). Parcels were included if the array was sensitive to at least 50% of the GM surface mesh nodes belonging to that parcel (as determined by the GM sensitivity mask, see above) and across at least twelve out of fourteen sessions (85%). These parameters were the highest possible values for number of sessions and nodes that still included full cortical coverage over the regions of interest. Once the sensitivity profile of the system was applied to the parcellated cortex, 154 parcels remained within the field-of-view of our experiment (**Fig. 3**).

2.7. Parcel assignment to resting state functional connectivity networks

Following parcellation, parcels were clustered into RSFC networks as described by Yeo et al. (2011, below referred to as **Yeo Networks**). [Thomas Yeo et al., 2011] This was performed to visualize which RSFC networks the array was sensitive to; serve as the ground truth for our spatial ICA analysis (see **Section 2.8.1**); and allow for the assessment of individual RSFC networks in our similarity and reliability analyses (see **Section 2.8.2**). The Yeo Networks were originally identified using resting state fMRI in 1000 adult subjects, and define the spatial cortical maps of the brain's RSFC networks. [Thomas Yeo et al., 2011] The Schaefer parcellation scheme was developed based on the Yeo Networks, [Schaefer et al., 2018] such that each parcel has a corresponding Yeo Network. For this dataset, the 154 Schaefer parcels that our HD-DOT system was sensitive to were assigned to Yeo Networks based on their spatial overlap. On this basis, our system was sensitive to six Yeo Networks: the visual central network, the visual peripheral network, dorsal attention network, salience network, the control, and the default mode network (DMN). These networks were split into left and right hemispheres for analysis purposes but are presented as unified in **Fig. 3**.

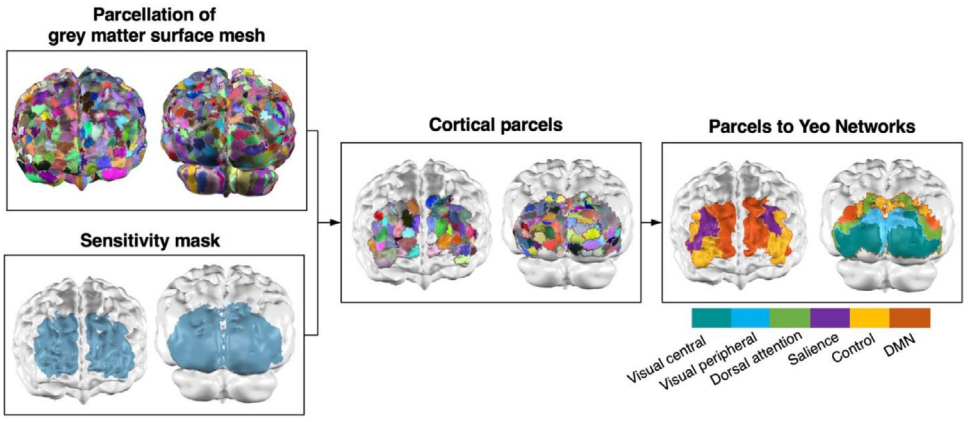

Fig. 3. Cortical parcellation and parcel assignment to resting state functional connectivity networks. Parcellation of the subject's grey matter surface mesh according to the Schaefer parcellation scheme was combined with the binary sensitivity mask of the 24-module array. Remaining parcels after application of the sensitivity mask to the parcellated grey matter surface mesh were clustered according to the Yeo Networks. Each parcel was included in one of six Yeo Networks (visual central, visual peripheral, dorsal attention, salience, control, and default mode network) to which the system was sensitive. (For interpretation of the references to colour in this figure legend, the reader is referred to the web version of this article.)

2.8. Functional connectivity analyses

2.8.1. Spatial group independent component analysis (sGICA)

Group-level RSFC networks were computed by means of a spatial group ICA [Beckmann et al., 2009] by temporally concatenating all recording sessions' datasets after time-series normalization to zero mean and unit variance, producing a single group dataset with dimensions [parcels x haemoglobin chromophores (2)] x [time points x fourteen sessions]. The FastICA algorithm [Hyvarinen, 1999] was applied to the group dataset to extract 21 independent components (ICs). This number was chosen because it is equal to the number of principal components that explain 70% of the group data variance. These parameters are based on the consistency of the ICA components across multiple realizations of the algorithm and the temporal anti-correlation of HbO and HbR maps. [Blanco et al., 2021] The results of this sub-analysis are presented for completeness in **Supplementary Figure 5**. The session-specific spatial maps associated with each of the 21 independent RSFC networks were obtained using a dual-regression approach. This two-step method involves an initial spatial regression of the sGICA maps of interest against the session-specific dataset to obtain the session-specific time courses associated with each group-level IC. Then, that time course is used as a regressor in a simple linear model to estimate session-specific spatial maps. T-stat maps were computed based on these session-specific spatial maps and multiple comparisons correction was performed using the Bonferroni method.

To avoid the subjective selection of IC maps to represent RSFC maps, we identified RSFC maps by quantitatively comparing them with the Yeo Networks using a Dice coefficient (**Fig. 4**). We used permutation testing to ascribe a p-value to the obtained Dice coefficients for each network. To create a null distribution, we computed 1000 permutations, where for each permutation the location of parcel labels was randomly exchanged in each session's dataset. This resulted in a 'parcel-label randomized dataset'. Then, the parcel-label randomized dataset was input to sGICA as described in the paragraph above. Following each iteration of sGICA, the Dice coefficient was computed for each spatial map and the associated Yeo Networks. The maximum Dice coefficient, representing the spatial map with highest overlap with any of the Yeo Networks, was stored to create an empirical estimate of the null distribution of maximal values. Finally, we estimated the p-value of the Dice coefficient associated with each network as the number of values in the null distribution that are larger than the observed value divided by the total number of permutations.

2.8.2. Assessment of similarity across sessions and reliability across scanning durations

In the fMRI literature, precision functional connectivity mapping (PFM) is a technique that can be used to characterize the similarity of FC network features of individual brains across recording sessions (i.e., how spatially consistent the identified networks are from session to session, day to day) and the reliability across recording durations (i.e. how stable networks are as a function of the duration of the dataset used to resolve them). [Gordon et al., 2017, Lynch et al., 2020] PFM considers large quantities RSFC data obtained from individual subjects (such as through multiple scanning sessions or a single multi-hour session) as opposed to collecting single-session, short-duration data from multiple subjects in a group. [Gordon et al., 2017, Lynch et al., 2020, Gratton et al., 2020] The subject is considered 'densely sampled', in a manner equivalent to collecting single datasets from multiple individuals. For example, Laumann et al. (2015) analysed 84 sessions of resting-state fMRI data of a single individual and found networks to be highly similar across sessions within the sampled individual. [Laumann et al., 2015] Relatedly, Gordon et al. (2017) investigated the reliability of RSFC matrices and a set of graph theory metrics (e.g., global efficiency and modularity) across a range of scanning durations and found that the scanning duration required to obtain a reliable characterization varied from 10 to 90 minutes depending on the measure. [Gordon et al., 2017]

Here, the computation of RSFC network *similarity* was adapted from PFM approaches employed by Gordon et al. (2017) and Laumann et al. (2015). [Gordon et al., 2017, Laumann et al., 2015] First, for each session, we generated a parcel-to-parcel FC matrix. This involved calculating the correlation (Pearson correlation coefficient, r) between each parcel's time-course and the time-courses of all other parcels, effectively providing a 154 × 154 FC matrix for each session, and for both HbO and HbR. Then, for each session, a 'ground truth' FC matrix was calculated based on the concatenated data of all 13 of the other sessions (note we use the term 'ground truth' here as defined in previous studies [Lynch et al., 2020] for consistency). Next, we divided individual and ground truth FC matrices into networks, such that each new 'network' matrix contained only the parcels that fell within that network. To compute the similarity matrix for each network, we vectorized the upper triangular part of the session specific FC matrix and its corresponding ground truth, performed Fisher's r-to-z transformation to improve normality, and computed the correlation of vectorized functional connectivity matrix within a given session with vectorized FC matrices of all other sessions and with the session specific ground truth. The resulting matrix is symmetric, with dimensions (14 sessions + 1 ground truth) x (14 sessions + 1 ground truth). Similarity matrices were computed for each of the six RSFC networks and for the complete connectome that included all parcels.

In addition, the computation of RSFC network *reliability*, as a function of recording duration, was adapted from the PFM approach employed by Lynch et al. (2020). [Lynch et al., 2020] For each session, a parcel-to-parcel RSFC matrix was calculated for each network (and for the complete connectome) using data segments of length one to twelve

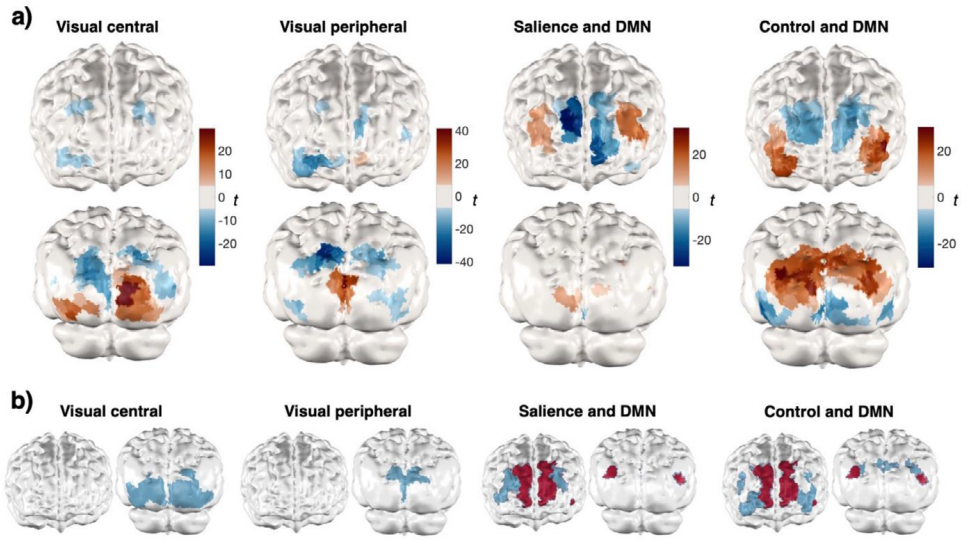

Fig. 4. Networks derived from spatial group independent component analysis (HbO). a) Each column displays the spatial map from the extracted independent components (IC). ICs were selected based on their stability over multiple realizations of the FastICA algorithm. Maps are presented as Bonferroni-corrected t-stat maps. b) Spatial maps corresponding to the Yeo visual central network, Yeo visual peripheral network, Yeo salience network and Yeo DMN, and Yeo control network and Yeo DMN (dark red). Scientific colormaps [Crameri et al., 2020] used for t-stat maps and in below figures. (For interpretation of the references to colour in this figure legend, the reader is referred to the web version of this article.)

minutes (the full duration of each session). These blocks were extracted using a sliding window approach with a step of 30 seconds. This approach generated different numbers of data blocks for each recording duration (e.g., 23 blocks of one minute duration, one block of twelve-minute duration per session). For each data block, the associated RSFC maps were compared with the corresponding ground truth matrix created using the complete concatenated data of all other sessions as described above. Reliability was calculated for the complete connectome and for each network as the average spatial correlation (R^2) between individual session and ground truth RSFC maps after Fisher's r-to-z transformation. While Laumann et al. (2015) and Gordon et al. (2017) used Pearson's r as a measure of reliability, we chose to use R^2 as per Lynch et al. (2020). Thus, high and low reliability values indicate that the FC of a specific network, using the specified amount of data from a single session, was similar or dissimilar to FC of that same network when calculated using a large amount of independent data. Reliability curves were obtained by finding the median reliability score of all data segments extracted at each recording duration and across testing sessions. Finally, we also computed the percent change in reliability between consecutive time windows (e.g., one minute time window vs. two minutes time window).

3. Results

3.1. Spatial group ICA demonstrates the presence of prominent RSFC networks

The RSFC networks obtained via the spatial group ICA analysis are presented in Fig. 4. RSFC networks were selected based on their spatial configuration and overlap with the Yeo Networks based on the Dice coefficient. Due to the high similarity between HbO and HbR maps, HbO maps are presented in the main text and HbR maps are presented in supplementary materials (see **Supplementary Figure 6**). RSFC networks are depicted as Bonferroni-corrected t-stat maps, which were computed from one-sample t-tests on the session-specific reconstructed spatial maps in the parcel space (using the dual-regression approach described above). The observed components were robust across multiple realizations of the ICA algorithm (see **Supplementary Figure 5**).

The first spatial map presented in Fig. 4 was identified as the visual central network due to its prominence in the central visual field and spatial overlap with the Yeo visual central network (HbO Dice coefficient = 0.61, $p<0.001$). There is clear asymmetry in this network in this subject, with a larger component apparent in the right visual network. However, this is consistent with the observed stronger right hemisphere visual field activation in the same subject in response to a rotating visual stimulus in our prior study. [Vidal-Rosas et al., 2021] The second plot displays an spatial map that was labelled as the visual peripheral network for its strong anatomical overlap with the Yeo visual peripheral network (HbO Dice coefficient = 0.49, $p = 0.001$). The third spatial map shows a symmetric pattern over the dorsolateral pre-frontal cortex, associated with the salience network that is anticorrelated with a symmetric, strongly significant pattern over the anterior pre-frontal cortex, belonging to the DMN (HbO Dice coefficients for salience = 0.48, $p = 0.001$, for DMN = 0.7, $p<0.001$). The last plot shows a spatial map over the ventrolateral pre-frontal cortex and parietal lobule, overlapping with the Yeo control network, which is anticorrelated with a symmetric pattern over the anterior pre-frontal cortex that is consistent with the Yeo DMN (HbO Dice coefficient for control = 0.52, $p<0.001$, for DMN = 0.48, $p = 0.001$). None of the extracted IC maps showed a significant spatial overlap with the Yeo dorsal attention network.

3.2. Similarity and reliability of RSFC network features

Individual parcel-based FC matrices for each session were used for similarity. Fig. 5 presents the averaged group-level FC matrix with parcels ordered according to the Yeo Networks. Example of individual session FC matrices are presented in supplementary materials (**Supplementary Figures 1–4**). For each Yeo Network, the total number of parcels included was: visual central, 44; visual peripheral, 13; dorsal attention, 26; salience, 14; control, 29; default mode, 28. At the group level, off-diagonal correlations are evident (see green arrows in Fig. 5), as are interhemispheric correlations within network across hemispheres (see dashed yellow squares in Fig. 5).

Fig. 6**a** presents the similarity matrix as computed from all parcels across all sessions with results for both HbO and HbR. The values on the diagonal indicate the correlation of each session with itself, and off-diagonal values indicate a given session's correlation with all other sessions or the session-independent ground truth (last column and last row). This plot indicates high similarity between sessions for both chromophores, with inter-session FC matrix correlations typically exceeding 0.79 for HbO and 0.78 for HbR, and correlation with the session-independent ground truth averaging 0.64 for HbO and 0.64 for HbR. Fig. 6**b and 6c** show the reliability values computed for each session and across data blocks of different durations, for the FC matrices including all parcels. These figures describe how similar the FC matrices are when calculated from different recording durations versus using large amounts of data from the session-independent ground truth. Results show that reliability scores increase with recording duration. Here,

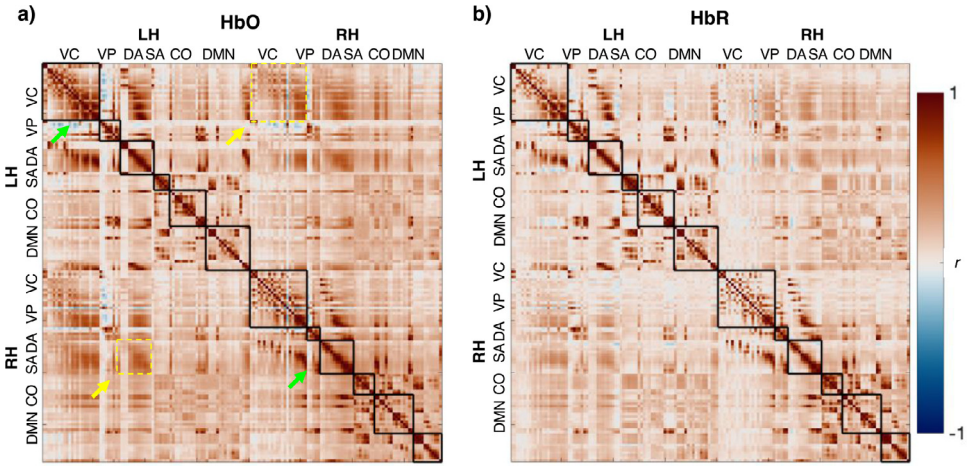

Fig. 5. Group-level functional connectivity matrix. Group-level (all session) functional connectivity matrix with parcels ordered according to Yeo Networks and divided into left (LH) and right (RH) hemispheres for HbO (a) and HbR (b). Black squares along the diagonal indicate parcels as they belong to each Yeo Network. Abbreviations: visual central (VC), visual peripheral (VP), dorsal attention (DA), salience (SA), control (CO), and default mode (DMN) networks. Dashed yellow squares and yellow arrows indicate apparent structure in network connectivity between the contralateral hemispheres for HbO (i.e. strong correlation between the left and right hemisphere for the visual central network in the upper yellow box, and between the left and right hemisphere for the dorsal attention network in the lower yellow box). Green arrows indicate networks with strong off diagonal correlations for HbO. (For interpretation of the references to colour in this figure legend, the reader is referred to the web version of this article.)

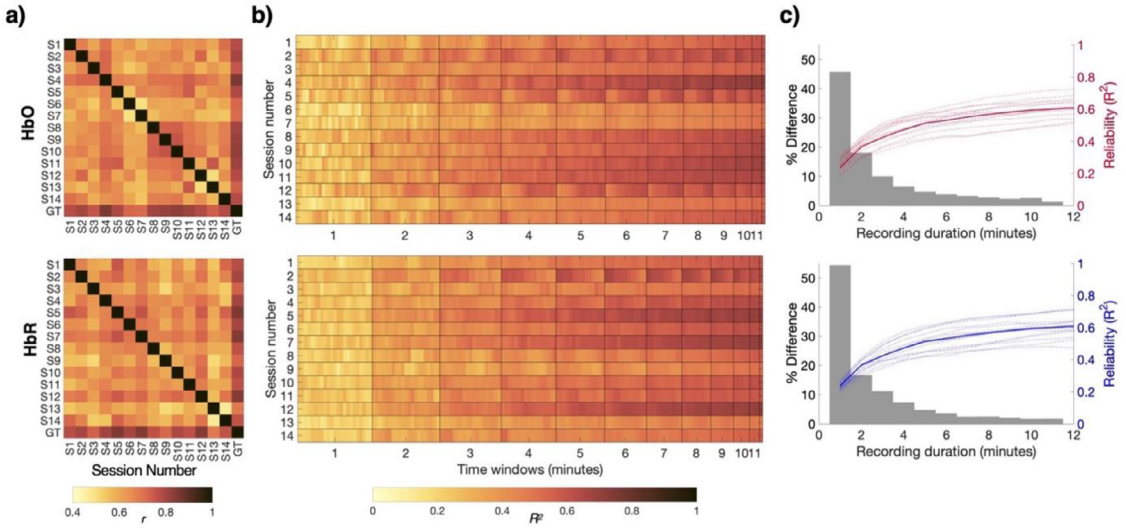

Fig. 6. Similarity and reliability of functional connectivity across all networks. a) Similarity across sessions for the complete connectome including all parcels and with session-independent ground truth functional connectivity matrix for HbO (upper row) and HbR (lower row); b) Reliability index for each session displayed as a function of the length of data used to compute the functional connectivity matrix. This index is based on the spatial correlation between functional connectivity matrices using varying data durations from an individual session and the session-independent ground truth (GT) functional connectivity matrix. c) Reliability curves for HbO (red lines and right y-axis) and HbR (blue lines and right y-axis). Values approaching 1 indicate better reliability. Dotted lines are session-specific reliability curves, and the solid line is the averaged curve for all sessions. On the same plot, grey bars represent the median percent difference in reliability values across consecutive time windows. (For interpretation of the references to colour in this figure legend, the reader is referred to the web version of this article.)

values approaching 1 indicate better reliability. The largest changes in reliability are observed within the first two minutes of the recording, after which, reliability values begin to plateau at around 4–5 minutes of data for most sessions. Overall, fairly reliable (>0.5) and stable values are obtained after this point, with the percent change in reliability between consecutive time windows (in grey) drops below 10% for both HbO and HbR.

Fig. 7 presents the similarity matrices and reliability curves separately for every RSFC network. Visual inspection of these figures demonstrates that some networks have greater stability across sessions, such as the visual peripheral network, dorsal attention network, DMN, and salience network, as compared to visual central and control networks. Nonetheless, all demonstrate high levels of similarity between sessions: inter-session correlation values ranged from 0.69 to 0.83 for all networks for HbO and from 0.73 to 0.88 for all networks for HbR (Table 1). This is also the case for each session compared with the ground truth: session-ground truth correlation values ranged from 0.82 to 0.91 for all networks for HbO and from 0.84 to 0.93 for all networks for HbR (Table 1). Reliability curves support these observations.

For reliability, similar outcomes are observed when considering each network separately as when using the complete FC matrix including all parcels. Overall, the largest increases in reliability scores are observed during the first two minutes, but the point in which reliability scores become relatively stable (i.e., a change <10% between consecutive time windows) varies across functional networks (Fig. 7). For example, the visual central network showed stable and fairly reliable (>0.5) values after three minutes recordings in HbO and four minutes in HbR. The visual peripheral network achieved this point at just two minutes (HbO and HbR) with values exhibiting high reliability (>0.8). In the dorsal attention network stable reliability values were achieved with two- and three-minute recordings for HbO and HbR respectively, with high reliability values (>0.7) observed after this point. In the salience network the largest changes in reliability values were observed during the first three minutes (HbO and HbR), reaching high reliability values (>0.7) during this period. The control network showed fairly reliable values

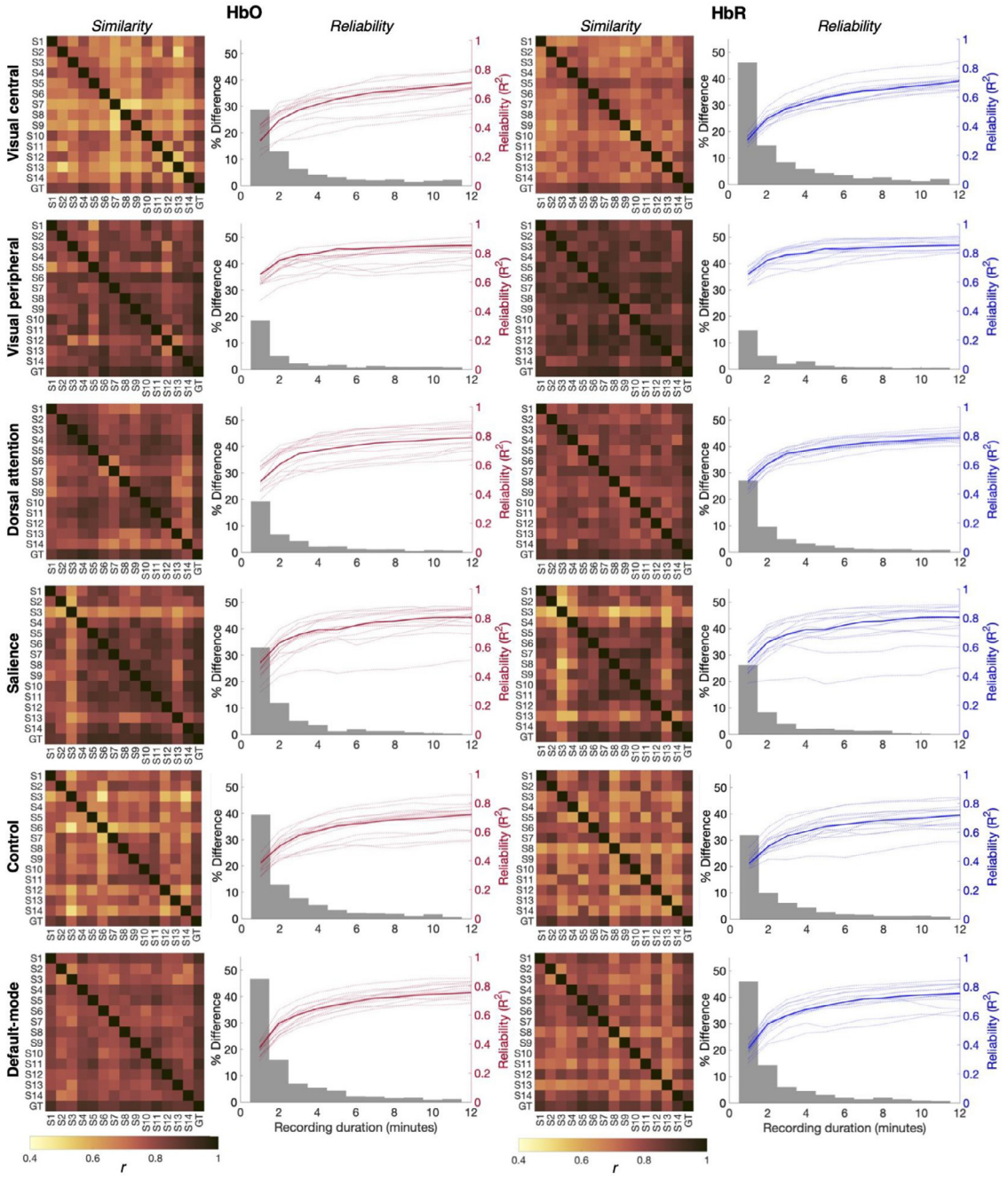

Fig. 7. Network-specific similarity and reliability plots. Similarity across sessions in six RSFC networks (each row represents a different RSFC network) and with session-specific ground truth (GT) functional connectivity matrix for HbO (first two columns) and HbR (third and fourth columns). To the right of each similarity matrix, the reliability curve for each session calculated for a set of time windows is displayed. Grey bars represent the median percent difference in reliability values across consecutive time windows.

Table 1
Session-to-ground truth (GT) and inter-session similarity values.

	Session-GT HbO mean [min – max]	Session-GT HbR mean [min – max]	Inter-session HbO mean [min – max]	Inter-session HbR mean [min – max]
Visual Central	0.82 [0.7 – 0.89]	0.84 [0.8 – 0.92]	0.69 [0.5 – 0. 82]	0.73 [0.61 – 0.82]
Visual Peripheral	0.91 [0.83 – 0.95]	0.93 [0.9 – 0.96]	0.83 [0.62 – 0.92]	0.88 [0.77 – 0.95]
Dorsal Attention	0.90 [0.8 – 0.95]	0.89 [0.85 – 0.93]	0.82 [0.66 – 0.93]	0.81 [0.73 – 0.89]
Salience	0.90 [0.71 – 0.93]	0.89 [0.68 – 0.94]	0.82 [0.58 – 0.92]	0.80 [0.52 – 0.95]
Control	0.84 [0.73 – 0.93]	0.85 [0.73 – 0.92]	0.73 [0.47 – 0.86]	0.74 [0.59 – 0.89]
DMN	0.88 [0.83 – 0.93]	0.87 [0.78 – 0.92]	0.80 [0.66 – 0.9]	0.77 [0.65 – 0.87]
All parcels	0.79 [0.72 – 0.85]	0.78 [0.69 – 0.85]	0.64 [0.5 – 0.76]	0.64 [0.47 – 0.76]

(>0.5) after four-minute recordings in HbO and after three minutes in HbR. Lastly, the DMN displayed the largest changes over the first three minutes for HbO and HbR, displaying reliability values of >0.5.

4. Discussion

Resting state functional connectivity mapping from densely sampled individuals can provide critical information about meaningful traits of the human brain, but this approach has not typically been performed in non-laboratory environments. Here, we used a wearable, 24-module HD-DOT system (LUMO, *Gowerlabs, Ltd.*) to assess the feasibility of collecting RSFC data in the home environment across multiple sessions over a period of three weeks during COVID-19 lockdown conditions. As an initial validation of our dataset, we used sGICA to identify the presence of RSFC networks and found them to be consistent with those previously identified in the fMRI literature. [Thomas Yeo et al., 2011] We investigated the similarity of identified RSFC networks across sessions, and the reliability of these networks across recording durations using techniques adapted from the fMRI literature. [Gordon et al., 2017, Lynch et al., 2020, Gratton et al., 2020] Our results demonstrate similarity across sessions of all investigated RSFC networks, and that fairly reliable results can be obtained at shorter scanning times, allowing some variation in minimum times across functional networks. This study represents the first demonstration on the use of wearable HD-DOT as a complimentary tool to fMRI for brain imaging in a non-laboratory environment. The technology and application described here have the potential to generate a wave of resting state functional brain imaging applications in non-traditional environments to study both neurotypical and neurodivergent populations of all ages.

One of the main aims of this study was to demonstrate that wearable HD-DOT could be used to obtain RSFC networks that demonstrated high similarity and reliability across imaging sessions. In assessing the similarity of networks, we observed that session-to-session RSFC networks were highly similar in this individual, with average inter-session correlation values ranging from $r = 0.64–0.83$ for HbO and $r = 0.64–0.88$ for HbR (**Table 1**). These reliability and similarity values are higher than those observed in the fMRI literature in the above cited studies that employed PFM approaches. For example, Lynch et al. 2020 showed values ($R^2 =\sim 0.2–0.6$) using 30 minutes of single-echo fMRI data, and Gordon et al. (2017) reported values ($R^2 =\sim 0.36–0.64$) using 30 minutes of single-echo fMRI data. Similar findings of network reproducibility have been previously reported as the basis for connectivity-based "fingerprinting" of individuals. [Anderson et al., 2011, Finn et al., 2015, Miranda-Dominguez et al., 2014, Xu et al., 2016] However, it is of note that direct comparisons between the findings here and the reported fMRI similarity values are not entirely appropriate as fMRI includes the entire cortical surface and subcortical regions. Therefore, while high similarity could be demonstrated using HD-DOT, this finding should be interpreted within its own methodological context. Additionally, while reproducibility was high, in this study some within-subject variability was also observed, with visual central and control networks demonstrating slightly lower average inter-session similarity values as compared to the DMN, salience, visual peripheral, and dorsal attention networks. This finding is consistent with those of Laumann et al. (2015), in which higher inter-session variability was observed in visual regions as compared to frontoparietal, default mode, and ventral attention regions.[48] Individual variability in RSFC network characteristics has been previously described as partially attributable to biological sources, such as diurnal rhythms [Hodkinson et al., 2014] and variations in metabolic state. [Rack-Gomer et al., 2009] However, in this study all sessions were performed at approximately the same time of day (between 10:00–12:00 BST), thus this likely was not a significant contributing effect. Sleep quality was not controlled for in this subject, which may have contributed to observed sources of variability. There may also have been subtle changes in how well the subject fixated on the central cross, which were not accounted for such as by using eye-tracking as a regressor. Moreover, numerous studies have demonstrated specific effects of different cognitive and behavioural contexts on resting-state activity. [Gordon et al., 2014, Tambini et al., 2010] These cognitive contexts could not be entirely controlled from session to session and therefore may have contributed to cross-session variability. Nonetheless, our results from this exploratory study suggest a high level of inter-session correlation and low cross-session variability overall.

In assessing the reliability of RSFC networks, we observed that fairly stable reliability values (stable described as a <10% change between time windows) could be obtained with relatively short recording durations. This finding demonstrates that longer scanning times may not always be necessary to study basic features of RSFC networks. When reliability curves were calculated for each network individually, some differences were noted in the minimum scanning time required to achieve stable reliability values. For example, the visual central, control and DMN showed stable reliability values after approximately four minutes of recording, while visual peripheral, dorsal and salience networks achieved this point during the first three minutes. It is of note that the visual central and control networks included a greater proportion of cortical surface ($n = 44$ parcels for visual central, $n = 29$ parcels for control) as compared to the visual peripheral ($n = 13$ parcels). It is possible that a greater scanning time is required to compensate for the greater number of parcels, and thus the greater number of potential sources of variability. Previous studies in the fMRI literature have also noted the rate at which measures of FC become reliable varies by brain region. [Lynch et al., 2020, Noble et al., 2017] In the context of this study, this may also be related to the sensitivity and associated signal-to-noise ratio, such that larger areas of the cortex will provide greater signal as compared to smaller or more shallow areas.

The other main aim of this study was to demonstrate that a wide field-of-view, wearable HD-DOT system can be used to perform functional brain imaging outside of the traditional laboratory environment. In this work, we implemented a wearable 24-module HD-DOT system that was sufficient to cover the full adult visual and pre-frontal cortices and perform functional brain imaging in the home environment. The performance capabilities are comparable to those of traditional fibre-based systems, [White et al., 2009, White and Culver, 2010] yet with significant advantages due to its wearable and ergonomic design. This system also provides a relatively large field of view for a HD-DOT device. However, it was still limited in its coverage, which restricts the number of RSFC networks we could interrogate. Here, we demonstrated the feasibility of using this system in the home environment over repeated sessions, yet other naturalistic environments may be of consideration. The ergonomics of this system also open new opportunities for repeated-session, individual-specific functional brain imaging for use in clinical applications (i.e., at the bedside) and for vulnerable populations (i.e., infants and young children).

The system described in this work is designed to allow for expansion to whole-head coverage, allowing for high density, full field-of-view HD-DOT of the human cortex. Indeed, our group is currently piloting a 54-tile version of this system. If demonstrated to be feasible, future studies may consider employing this whole-head version to probe the reliability and similarity of all RSFC networks across the superficial cerebral cortex in ecologically meaningful settings. Future studies should also consider multiple subjects for validation of this technique across multiple individuals (hampered here somewhat by COVID-19 circumstances), comparison with fMRI-based acquisition (also hampered by COVID-19 circumstances), and the addition of task-based imaging for demonstration of correspondence between resting-state and task-based FC. Another consideration is whether the decay of the reliability curves or the strength of the correlation values in the similarity matrices is related to the differential sensitivity of our array to these regions. Validation across different populations (infants, children, and clinical populations) is also a priority. To conclude, while much work is still needed, there is a multitude of possible applications of the methods and technology described here in diverse subject populations and ecological contexts.

Data availability statement

Data sharing unavailable under our UCL ethics protocol for protection of personal information.

Disclosures

This paper involves the application of a technology developed by Gowerlabs Ltd.

Data availability

The authors do not have permission to share data.

Credit authorship contribution statement

Julie Uchitel: Writing - Original draft, Methodology, Visualization, Formal analysis, Conceptualization, Writing - Reviewing and Editing. **Borja Blanco:** Conceptualization, Methodology, Formal analysis, Visualization, Writing - Original draft, Writing - Reviewing and Editing. **Ernesto Vidal-Rosas:** Methodology, Writing - Reviewing and Editing. **Liam Collins-Jones:** Methodology, Formal analysis, Writing - Reviewing and Editing. **Robert J Cooper:** Investigation – Data Collection, Supervision, Conceptualization, Methodology, Writing - Reviewing and Editing.

Acknowledgements

R. J. C. would like to acknowledge Andrea Zitna for her photogrammetry skills and patience. B. B. would like to acknowledge César Caballero-Gaudes for his support during the review process. J.U. was funded by a Marshall Scholarship and a Cambridge Trust Scholarship. R. J. C. was funded by Engineering and Physical Sciences Research Council fellowship (No. EP/N025946/1).

Supplementary materials

Supplementary material associated with this article can be found, in the online version, at doi:10.1016/j.neuroimage.2022.119663.

References

Damoiseaux, J.S., Rombouts, S A.RB, Barkhof, F., et al., 2006. Consistent resting-state networks across healthy subjects. Proc. Natl. Acad. Sci. U.S.A. 103 (37), 13848–13853. doi:10.1073/pnas.0601417103.

Fransson, P., Skiöld, B., Horsch, S., et al., 2007. Resting-state networks in the infant brain. Proc. Natl. Acad. Sci. U.S.A. 104 (39), 15531–15536. doi:10.1073/pnas.0704380104.

Betzel, R.F., Byrge, L., He, Y., Goñi, J., Zuo, X.N., Sporns, O., 2014. Changes in structural and functional connectivity among resting-state networks across the human lifespan. Neuroimage 102, 345–357. doi:10.1016/j.neuroimage.2014.07.067.

Honey, C.J., Sporns, O., Cammoun, L., et al., 2009. Predicting human resting-state functional connectivity from structural connectivity. PNAS 106 (6), 2035–2040. doi:10.1073/pnas.0811168106.

Beckmann, C.F., DeLuca, M., Devlin, J.T., Smith, S.M., 2005. Investigations into resting-state connectivity using independent component analysis. Philos. Trans. R. Soc. Lond. B Biol. Sci. 360, 1001–1013. doi:10.1098/rstb.2005.1634, (1457).

Smith, S.M., Fox, P.T., Miller, K.L., et al., 2009. Correspondence of the brain's functional architecture during activation and rest. Proc. Natl. Acad. Sci. U.S.A. 106 (31), 13040–13045. doi:10.1073/pnas.0905267106.

Thomas Yeo, B.T., Krienen, F.M., Sepulcre, J., et al., 2011. The organization of the human cerebral cortex estimated by intrinsic functional connectivity. J. Neurophysiol. 106 (3), 1125–1165. doi:10.1152/jn.00338.2011.

Boas, D.A., Elwell, C.E., Ferrari, M., Taga, G., 2014. Twenty years of functional near-infrared spectroscopy: introduction for the special issue. Neuroimage 85, 1–5. doi:10.1016/j.neuroimage.2013.11.033.

Racz, F.S., Mukli, P., Nagy, Z., Eke, A., 2018. Multifractal dynamics of resting-state functional connectivity in the prefrontal cortex. Physiol. Meas. 39 (2). doi:10.1088/1361-6579/aaa916, 024003.

Zhang, Y., Zhu, C., 2020. Assessing Brain Networks by Resting-State Dynamic Functional Connectivity: an fNIRS-EEG Study. Front. Neurosci. 13, 1430. doi:10.3389/fnins.2019.01430.

Niu, H., Zhu, Z., Wang, M., et al., 2019. Abnormal dynamic functional connectivity and brain states in Alzheimer's diseases: functional near-infrared spectroscopy study. Neurophoton 6 (02), 1. doi:10.1117/1.NPh.6.2.025010.

Li, Z., Liu, H., Liao, X., et al., 2015. Dynamic functional connectivity revealed by resting-state functional near-infrared spectroscopy. Biomed. Opt. Express 6 (7), 2337. doi:10.1364/BOE.6.002337.

Lu, C.M., Zhang, Y.J., Biswal, B.B., Zang, Y.F., Peng, D.L., Zhu, C.Z., 2010. Use of fNIRS to assess resting state functional connectivity. J. Neurosci. Methods 186 (2), 242–249. doi:10.1016/j.jneumeth.2009.11.010.

Niu, H., Li, Z., Liao, X., et al., 2013. Test-Retest Reliability of Graph Metrics in Functional Brain Networks: a Resting-State fNIRS Study. Sporns O. PLoS ONE 8 (9), e72425. doi:10.1371/journal.pone.0072425.

Homae, F., Watanabe, H., Otobe, T., et al., 2010. Development of global cortical networks in early infancy. J. Neurosci. 30 (14), 4877–4882. doi:10.1523/JNEUROSCI.5618-09.2010.

Taga, G., Watanabe, H., Homae, F., 2018. Developmental changes in cortical sensory processing during wakefulness and sleep. Neuroimage 178, 519–530. doi:10.1016/j.neuroimage.2018.05.075.

Blanco, B., Molnar, M., Carreiras, M., et al., 2021. Group-level cortical functional connectivity patterns using fNIRS: assessing the effect of bilingualism in young infants. Neurophoton 8 (02). doi:10.1117/1.NPh.8.2.025011.

Lee, C.W., Blanco, B., Dempsey, L., et al., 2020. Sleep State Modulates Resting-State Functional Connectivity in Neonates. Front. Neurosci. 14, 347. doi:10.3389/fnins.2020.00347.

Pinti, P., Tachtsidis, I., Hamilton, A., et al., 2020. The present and future use of functional near-infrared spectroscopy (fNIRS) for cognitive neuroscience. Ann. N. Y. Acad. Sci. 1464 (1), 5–29. doi:10.1111/nyas.13948.

White, B.R., Snyder, A.Z., Cohen, A.L., et al., 2009. Resting-state functional connectivity in the human brain revealed with diffuse optical tomography. Neuroimage 47 (1), 148–156. doi:10.1016/j.neuroimage.2009.03.058.

Eggebrecht, A.T., Ferradal, S.L., Robichaux-Viehoever, A., et al., 2014. Mapping distributed brain function and networks with diffuse optical tomography. Nature Photon 8 (6), 448–454. doi:10.1038/nphoton.2014.107.

Chalia, M., Dempsey, L.A., Cooper, R.J., et al., 2019. Diffuse optical tomography for the detection of perinatal stroke at the cot side: a pilot study. Pediatr. Res. 85 (7), 1001–1007. doi:10.1038/s41390-018-0263-x.

White, B.R., Culver, J.P., 2010. Quantitative evaluation of high-density diffuse optical tomography: in vivo resolution and mapping performance. J. Biomed. Opt. 15 (2). doi:10.1117/1.3368999, 026006.

Vidal-Rosas, E.E., Zhao, H., Nixon-Hill, R.W., et al., 2021. Evaluating a new generation of wearable high-density diffuse optical tomography technology via retinotopic mapping of the adult visual cortex. Neurophotonics 8 (2). doi:10.1117/1.NPh.8.2.025002, 025002.

Frijia, E.M., Billing, A., Lloyd-Fox, S., et al., 2021. Functional imaging of the developing brain with wearable high-density diffuse optical tomography: a new benchmark for infant neuroimaging outside the scanner environment. Neuroimage 225, 117490. doi:10.1016/j.neuroimage.2020.117490.

Geng, S., Liu, X., Biswal, B.B., Niu, H., 2017. Effect of Resting-State fNIRS Scanning Duration on Functional Brain Connectivity and Graph Theory Metrics of Brain Network. Front. Neurosci. 11, 392. doi:10.3389/fnins.2017.00392.

Wang, J., Dong, Q., Niu, H., 2017. The minimum resting-state fNIRS imaging duration for accurate and stable mapping of brain connectivity network in children. Sci. Rep. 7 (1), 6461. doi:10.1038/s41598-017-06340-7.

Zhao, H., Brigadoi, S., Brigadoi, S., et al., 2020. A wide field-of-view, modular, high-density diffuse optical tomography system for minimally constrained three-dimensional functional neuroimaging. Biomed. Opt. Express 11 (8), 4110–4129. doi:10.1364/BOE.394914, BOE.

Avants, B.B., Tustison, N.J., Song, G., Cook, P.A., Klein, A., Gee, J.C., 2011. A reproducible evaluation of ANTs similarity metric performance in brain image registration. Neuroimage 54 (3), 2033–2044. doi:10.1016/j.neuroimage.2010.09.025.

Ashburner, J., Friston, K.J., 2005. Unified segmentation. Neuroimage 26 (3), 839–851. doi:10.1016/j.neuroimage.2005.02.018.

31.iso2mesh. Accessed September 30, 2020. http://iso2mesh.sourceforge.net/cgi-bin/index.cgi?Home

Cooper, R.J., Selb, J., Gagnon, L., et al., 2012. A systematic comparison of motion artifact correction techniques for functional near-infrared spectroscopy. Front. Neurosci. 6, 147. doi:10.3389/fnins.2012.00147.

Sherafati, A., Snyder, A.Z., Eggebrecht, A.T., et al., 2020. Global motion detection and censoring in high-density diffuse optical tomography. Hum. Brain Mapp. 41 (14), 4093–4112. doi:10.1002/hbm.25111.

Gagnon, L., Cooper, R.J., Yücel, M.A., Perdue, K.L., Greve, D.N., Boas, D.A., 2012. Short separation channel location impacts the performance of short channel regression in NIRS. Neuroimage 59 (3), 2518–2528. doi:10.1016/j.neuroimage.2011.08.095.

Caballero-Gaudes, C., Reynolds, R.C., 2017. Methods for cleaning the BOLD fMRI signal. Neuroimage 154, 128–149. doi:10.1016/j.neuroimage.2016.12.018.

36.Arridge S.R. Optical tomography in medical imaging. Inverse Problems. 1999;15(2):R41–R93. doi:10.1088/0266-5611/15/2/022

Schweiger, M., Arridge, S., 2014. The Toast++ software suite for forward and inverse modeling in optical tomography. J. Biomed. Opt. 19 (4). doi:10.1117/1.JBO.19.4.040801, 040801.

Schweiger, M., Arridge, S., 2003. Image reconstruction in optical tomography using local basis functions. J. Electron. Imag. 12, 583–593. doi:10.1117/1.1586919.

Bevilacqua, F., Piguet, D., Marquet, P., Gross, J.D., Tromberg, B.J., Depeursinge, C., 1999. In vivo local determination of tissue optical properties: applications to human brain. Appl. Opt. 38 (22), 4939–4950. doi:10.1364/ao.38.004939.

40.Cope M. The Development of a near Infrared Spectroscopy System and Its Application for Non Invasive Monitoring of Cerebral Blood and Tissue Oxygenation in the Newborn Infants. Doctoral. University of London; 1991. Accessed January 6, 2021. https://discovery.ucl.ac.uk/id/eprint/1317956/

Schaefer, A., Kong, R., Gordon, E.M., et al., 2018. Local-Global Parcellation of the Human Cerebral Cortex from Intrinsic Functional Connectivity MRI. Cerebral Cortex 28 (9), 3095–3114. doi:10.1093/cercor/bhx179.

Collins, D.L., Neelin, P., Peters, T.M., Evans, A.C., 1994. Automatic 3D intersubject registration of MR volumetric data in standardized Talairach space. J. Comput. Assist. Tomogr. 18 (2), 192–205.

43.Beckmann C.F., MacKay C.E., Filippini N., Smith S.M. Group comparison of resting-state FMRI data using multi-subject ICA and dual regression. Published 2009. Accessed September 16, 2021. http://web.mit.edu/fsl_v5.0.10/fsl/doc/wiki/attachments/DualRegression/CB09.pdf

Hyvarinen, A., 1999. Fast and robust fixed-point algorithms for independent component analysis. IEEE Trans. Neural. Netw. 10 (3), 626–634. doi:10.1109/72.761722.

Gordon, E.M., Laumann, T.O., Gilmore, A.W., et al., 2017. Precision Functional Mapping of Individual Human Brains. Neuron 95 (4), 791–807. doi:10.1016/j.neuron.2017.07.011, e7.

Lynch, C.J., Power, J.D., Scult, M.A., Dubin, M., Gunning, F.M., Liston, C., 2020. Rapid Precision Functional Mapping of Individuals Using Multi-Echo fMRI. Cell. Rep. 33 (12), 108540. doi:10.1016/j.celrep.2020.108540.

Gratton, C., Kraus, B.T., Greene, D.J., et al., 2020. Defining Individual-Specific Functional Neuroanatomy for Precision Psychiatry. Biol. Psychiatry 88 (1), 28–39. doi:10.1016/j.biopsych.2019.10.026.

Laumann, T.O., Gordon, E.M., Adeyemo, B., et al., 2015. Functional System and Areal Organization of a Highly Sampled Individual Human Brain. Neuron 87 (3), 657–670. doi:10.1016/j.neuron.2015.06.037.

Crameri, F., Shephard, G.E., Heron, P.J., 2020. The misuse of colour in science communication. Nat. Commun. 11 (1), 5444. doi:10.1038/s41467-020-19160-7.

Anderson, J.S., Ferguson, M.A., Lopez-Larson, M., Yurgelun-Todd, D, 2011. Reproducibility of Single-Subject Functional Connectivity Measurements. AJNR Am. J. Neuroradiol. 32 (3), 548–555. doi:10.3174/ajnr.A2330.

Finn, E.S., Shen, X., Scheinost, D., et al., 2015. Functional connectome fingerprinting: identifying individuals using patterns of brain connectivity. Nat. Neurosci. 18 (11), 1664–1671. doi:10.1038/nn.4135.

Miranda-Dominguez, O., Mills, B.D., Carpenter, S.D., Hayasaka, S., et al., 2014. Connectotyping: model Based Fingerprinting of the Functional Connectome. PLoS ONE 9 (11), e111048. doi:10.1371/journal.pone.0111048.

Xu, T., Opitz, A., Craddock, R.C., Wright, M.J., Zuo, X.N., Milham, M.P., 2016. Assessing Variations in Areal Organization for the Intrinsic Brain: from Fingerprints to Reliability. Cereb. Cortex 26 (11), 4192–4211. doi:10.1093/cercor/bhw241.

Hodkinson, D.J., O'Daly, O., Zunszain, P.A., et al., 2014. Circadian and Homeostatic Modulation of Functional Connectivity and Regional Cerebral Blood Flow in Humans under Normal Entrained Conditions. J. Cereb. Blood Flow Metab. 34 (9), 1493–1499. doi:10.1038/jcbfm.2014.109.

Rack-Gomer, A.L., Liau, J., Liu, T.T., 2009. Caffeine reduces resting-state BOLD functional connectivity in the motor cortex. Neuroimage 46 (1), 56–63. doi:10.1016/j.neuroimage.2009.02.001.

Gordon, E.M., Breeden, A.L., Bean, S.E., Vaidya, C.J., 2014. Working memory-related changes in functional connectivity persist beyond task disengagement: persistent Changes in Functional Connectivity. Hum. Brain Mapp. 35 (3), 1004–1017. doi:10.1002/hbm.22230.

Tambini, A., Ketz, N., Davachi, L., 2010. Enhanced Brain Correlations during Rest Are Related to Memory for Recent Experiences. Neuron 65 (2), 280–290. doi:10.1016/j.neuron.2010.01.001.

Noble, S., Spann, M.N., Tokoglu, F., Shen, X., Constable, R.T., Scheinost, D., 2017. Influences on the Test–Retest Reliability of Functional Connectivity MRI and its Relationship with Behavioral Utility. Cerebral Cortex 27 (11), 5415–5429. doi:10.1093/cercor/bhx230.